

Flow Characteristics of a Dual-Intake Port Diesel Engine with Guide Vanes

Y. Z. Guo¹, H. L. Kui^{2†}, C. S. Shao¹, Z. Z. Wang¹, Y. Liu¹

¹ College of Transportation, Jilin University, Changchun 130022, China

² College of Biological and Agricultural Engineering, Jilin University, Changchun 130022, China

†Corresponding Author Email: khl69@163.com

(Received July 16, 2021; accepted December 12, 2021)

ABSTRACT

The intake port of a CA4DD diesel engine was investigated by a computational fluid dynamics (CFD) numerical simulation to enhance the intake swirl and improve the flow characteristics in the engine. The uniform design method was applied to study the influence of guide vanes with different parameters on the intake process at various valve lifts. Nine guide vane models were established and compared to the base model using CATIA™ 3D CAD software. Numerical simulations were conducted with Xflow software based on the lattice Boltzmann method (LBM). The distributions of the streamlines, vorticity, velocity and turbulent intensity in each cylinder were simulated and analyzed. The results show that the influence of the guide vanes on the swirl ratio was greater than 37%, and the flow coefficient was less than 5% compared to the base model. Scheme 5, H7.5-L50-020 (guide vane height of 7.5 mm, length of 50 mm and angle of 20°), provided good performance. The flow characteristics of the optimal guide vane model were verified through a steady flow test. When the guide vane aspect ratio and angle were within the ranges of 3.5-6.9 and 12.2°-20.2°, respectively, the swirl ratio had the best effect at maximum valve lift. This study provides a theoretical basis for improving the performance of dual-intake diesel engines.

Keywords: Diesel engine; Numerical simulation; Guide vane; Uniform design; Steady flow test.

NOMENCLATURE

3D	three-dimensional	n_D	swirl rotational speed
BGK	Bhatnagar-Gross-Krook	Q	volume flow
CFD	computational Fluid Dynamics	Re	Reynolds Number
LBM	Lattice Boltzmann Method	r	particle position
LES	Large Eddy Simulation	t	physical time
SGS	Sub-Grid Scale	u	fluid velocity
WALE	Wall-Adapting Local Eddy-Viscosity	u'	root-mean-square of the turbulent velocity fluctuations
A_{inlet}	inlet area	U	mean velocity
C_ω	wall-adapting local eddy-viscosity constant	V	grid volume
C_f	flow coefficient	V_n	normal velocity to the surfaces of inlet
D_e	equivalent diameter	δ_t	time step
e_α	discrete velocities	ν_t	eddy viscosity
f_α	density distribution function	ρ	fluid density
f_α^{eq}	equilibrium distribution function	τ	dimensionless relaxation time
F_α	external force	τ_0	relaxation time
$G_{\alpha\beta}^d$	strain rate tensor	ω	vorticity
I	turbulence intensity		
k	turbulent kinetic energy		
m	inlet mass flow		
N_s	swirl ratio		
		Subscripts	
		x	physical component in x-direction
		y	physical component in y-direction
		z	physical component in z-direction

1. INTRODUCTION

Two important goals of scientific and technological development are to reduce energy consumption and environmental pollution. At present, the diesel engines used in vehicles are mainly small and medium-sized high-speed models, most of which use semi-open combustion chambers and need strong intake swirls (Kui *et al.* 2014). Strong intake swirl and good airflow in a cylinder can enhance the turbulence intensity of the oil-gas mixture and make it more uniform, which improves combustion (Leung and Wang 2000). In recent years, many domestic and foreign scholars have conducted extensive research to improve swirl. For example, Xin *et al.* (2012) proposed a new design of a variable swirl system with an adjustable swirl baffle in the intake manifold. Bari *et al.* studied guide vanes installed in front of the intake manifold of a single intake port diesel engine to improve the flow characteristics and analyzed the influence of vane length (Bari and Saad 2016), angle (Bari and Saad 2015b), height (Bari and Saad 2014) and number (Bari and Saad 2015a), on the flow characteristics and emissions of the engine. However, their research studied only a single-parameter and single-intake port diesel engine. These studies did not consider the interference between various guide vane parameters.

The strong intake swirl generated during the intake process can last until the later stage of the compression stroke (Wang *et al.* 2015). Intake swirl and fuel injection play important roles in fuel-air mixing and combustion of diesel fuel (Wang *et al.* 2020). This study focuses on the study of intake swirl. Guide vanes generate strong intake swirls that can improve combustion and reduce emissions. This paper comprehensively considered interference between the length, height, and angle of guide vanes, unlike the available literature that considers the influence of only a single factor on the engine. After comprehensive consideration of the interaction of guide vane parameters, three factors (guide vane length, height and angle) were each divided into 9 levels. The uniform design method, which ensures uniform distribution of the test points, was adopted to arrange the test scheme and determine the 9 groups of guide vane schemes. The guide vanes were applied to the dual-intake port diesel engine for research. Furthermore, the range of optimal values for vane parameters under maximum valve lift was determined. Guide vanes with different parameters were installed at the front end of the helical intake port of a dual-intake diesel engine to study the influence of guide vanes on flow characteristics. The intake-cylinder models were established by CATIA (computer-aided three-dimensional interactive application) software. The CFD (computational fluid dynamics) numerical simulation was carried out by the LBM (lattice Boltzmann method) based on kinetic theory. The swirl ratio and flow coefficient for different valve lifts were analyzed quantitatively. The optimum ranges of the guide vane parameters for maximum valve lift were determined. The flow field characteristics of velocity, vorticity and turbulence in cylinders were analyzed qualitatively. Finally, the simulation results were verified by a

steady flow test. The airflow configurations or mechanisms differ for various valve lifts (Bayramoglu *et al.* 2019; Li *et al.* 2012). The airflow adheres to the valve surface for small valve lift. As the valve lift increases, the fluid gradually separates from the wall (Szpica 2020). Consequently, this study focuses on the flow characteristics of high valve lifts (6, 8, and 10 mm) with different guide vanes.

2. METHODOLOGY

2.1 Design of the test scheme

This study focuses on the CA4DD diesel engine, which has helical and tangential dual intake ports. Table 1 shows the specifications of the CA4DD diesel engine. The helical intake port mainly produces intake swirls. Therefore, guide vanes were installed in the front of the helical intake port. In the simulation, it is assumed that each cylinder works uniformly. The test studies only single-cylinder flow. This paper established a simulation model with a single cylinder and double-intake port through CATIA.

Table 1 Engine specifications

Specification	Value
Valve number	4
Cylinder number	4
Bore/mm	95.4
Stroke/mm	104.9
Compression ratio	17:1
Intake valve diameter/mm	29.55
Rated speed/rpm	3200
Displacement/L	2.999
Intake port	Helical, tangential
Cylinder arrangement	Inline

The simulation model mainly consists of four parts: a stable pressure box, intake port, intake valve and cylinder (Jia *et al.* 2018). The stable pressure box simulates the external environment and facilitates subsequent calculations to impose boundary conditions. The shape and size of the simulation model are drawn strictly in accordance with the actual diesel engine. The cylinder is extended to 2.5 times that of the original model, which helps to reduce backflow at the outlet and makes the simulation converge (Jia *et al.* 2019). Theoretically, the intake time and exhaust time account for 180° of crankshaft angle rotation. Because the intake process is simulated, the exhaust valve and exhaust port are omitted from the simulation, which is conducive to saving computing resources. A schematic diagram of the guide vanes and their installation position is shown in Fig. 1.

There are five guide vane parameters: height, length, angle, number and thickness. These parameters interfere with each other. Considering the shape of the front end of the intake, the number of guide vanes

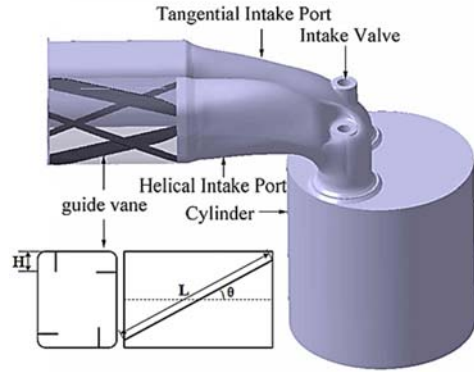


Fig. 1. Guide vanes and their installation in the base model.

was 4, and their thickness was 0.1 mm. The other three parameters were studied by uniform design. Uniform design optimization experiments have been widely used in various fields, and the test points generated by uniform design are evenly distributed within the test range, which greatly reduces the number of experiments (Leung and Wang 2000, Liu *et al.* 2012, Zhang *et al.* 2019). Based on previous studies (Bari and Saad 2014, Bari and Saad 2015a, Bari and Saad 2015b, Bari and Saad 2016), the guide vane height (H), length (L) and angle (θ) were taken as the test factors of uniform design. Additionally, the vane height varied between 1.5 and 13.5 mm with steps of 1.5 mm; the vane length varied between 30 and 70 mm with steps of 5 mm; and the angle varied between 4° and 36° with steps of 4° . The number of levels per factor was nine, and the test index was the swirl ratio. According to the factors and levels of the design, we defined the Table 2 by uniform design table. The details can be found in the literature (Fang *et al.* 2018). Table 3 was obtained by using the table of uniform design using vane height, length and angle. The numbers in parentheses are the level numbers of the factors. The numbers outside parentheses are the corresponding level the values of the factors. This paper determined the uniformly dispersed vane combination parameters in this test. The guide vanes were installed in front of the helical intake port of the base model. Guide vane models with different parameters were established. The values of the height, length and angle of the guide vanes were comprehensively studied. For convenience, the base model without guide vanes was identified as 0 and the guide vane models were numbered from 1 to 9. Different schemes were named according to their height-length-angle. For example, as shown in Table 1, scheme 1 was referred to as H1.5-L60- θ 36 (reflecting a guide vane height of 6 mm, length of 65 mm and angle of 24°). Other schemes have similar naming methods.

2.2 Mathematical model

This paper used Xflow software to simulate the intake process of a dual-intake port diesel engine with guide vanes using the LBM method, based on a simplified Boltzmann equation of kinetic theory, and describe flow phenomena on a mesoscopic scale that

Table 2 Factor level table

Level number	Factors		
	Height, mm	Length, mm	Angle, $^\circ$
1	1.5	30	4
2	3.0	35	8
3	4.5	40	12
4	6.0	45	16
5	7.5	50	20
6	9.0	55	24
7	10.5	60	28
8	12.0	65	32
9	13.5	70	36

Table 3 Uniform design scheme

Scheme number	Parameters		
	Height, mm	Length, mm	Angle, $^\circ$
1	(1)1.5	(7)60	(9)36
2	(2)3.0	(4)45	(8)32
3	(3)4.5	(1)30	(7)28
4	(4)6.0	(8)65	(6)24
5	(5)7.5	(5)50	(5)20
6	(6)9.0	(2)35	(4)16
7	(7)10.5	(9)70	(3)12
8	(8)12.0	(6)55	(2)8
9	(9)13.5	(3)40	(1)4

is between macroscopic and microscopic scales (Liu *et al.* 2021). Based on the simulation of microscopic particles, the interaction of fluids can be handled conveniently and intuitively. From the perspective of calculation, the evolution process is physically clear, and the calculation is simple. Its parallelism and scalability have great advantages for the calculation of complex turbulent flows and have been widely used (Han *et al.* 2019; Haussmann *et al.* 2020; Jonnalagadda *et al.* 2021; Sharma *et al.* 2020).

The controlling equation is filtered through the N-S (Navier-Stokes) equation (Long *et al.* 2019). The LBM is used to describe the motion of gas molecules through discretization. The continuous medium is regarded as discrete fluid particles located on the grid nodes. The particles move on the grid according to the collision and migration rules. We can obtain the macroscopic law of motion on the basis of molecular kinematics and statistics (Gao *et al.* 2021; Kumar *et al.* 2017). The lattice Boltzmann equation is a special discrete form of the Boltzmann-BGK equation, which includes discrete velocity, time and space (Evans *et al.* 2019; Xiao and Frank 2021). By the Bhatnagar-Gross-Krook (BGK) approximation, the lattice Boltzmann-BGK equation with an external force term is:

$$\begin{aligned}
 & f_\alpha(r + e_\alpha \delta_t, t + \delta_t) - f_\alpha(r, t) \\
 &= -\frac{1}{\tau} [f_\alpha(r, t) - f_\alpha^{eq}(r, t)] + \delta_t F_\alpha(r, t)
 \end{aligned}
 \tag{1}$$

where $f_\alpha(r, t)$ is the particle distribution function; e_α is the discrete velocity; δ_t is the time step; $\tau = \tau_0 / \delta_t$ represents the dimensionless relaxation time; τ_0 is the relaxation time; $f_\alpha^{eq}(r, t)$ represents the local equilibrium distribution function in discrete velocity space; and $F_\alpha(r, t)$ is the external force.

The macroscopic fluid density and velocity are calculated by Eq. (2) and Eq. (3), respectively.

$$\rho = \sum_\alpha f_\alpha = \sum_\alpha f_\alpha^{eq} \quad (2)$$

$$\rho u = \sum_\alpha e_\alpha f_\alpha = \sum_\alpha e_\alpha f_\alpha^{eq} \quad (3)$$

where ρ is the fluid density and u is the fluid velocity.

2.3 Turbulence model

In XFLOW, the turbulence model adopts a large eddy simulation (LES). The key aspect of the turbulence model is to solve the subgrid scale (SGS) stress term. This study uses the wall-adapting local eddy-viscosity model (WALE). The WALE model has good properties both near and far from the wall and for both laminar and turbulent flows (Tiwari *et al.* 2020). This model recovers the asymptotic behavior of the turbulent boundary layer when this layer can be directly solved, and it does not add artificial turbulent viscosity in the shear regions outside of the wake. The WALE model is formulated as follows:

$$v_t = \Delta^2 \frac{(G_{\alpha\beta}^d G_{\alpha\beta}^d)^{3/2}}{(S_{\alpha\beta}^d S_{\alpha\beta}^d)^{5/2} + (G_{\alpha\beta}^d G_{\alpha\beta}^d)^{5/4}} \quad (4)$$

$$\text{where } \begin{cases} S_{\alpha\beta} = \frac{1}{2} \left(\frac{\partial v_\alpha}{\partial r_\beta} + \frac{\partial v_\beta}{\partial r_\alpha} \right) \\ G_{\alpha\beta}^d = \frac{1}{2} (g_{\alpha\beta}^2 + g_{\beta\alpha}^2) - \frac{1}{3} \delta_{\alpha\beta} g_{\gamma\gamma}^2, \quad v_t \text{ denotes} \\ g_{\alpha\beta} = \frac{\partial v_\alpha}{\partial r_\beta} \\ \Delta = C_\omega V^{1/3} \end{cases}$$

the eddy-viscosity under the subgrid scale standard; Δ represents the filter scale; the WALE constant (C_ω) is typically 0.2; $G_{\alpha\beta}^d$ is the strain rate tensor on the analytical scale; and V represents the grid volume.

Under this turbulence model, the turbulence intensity I (in %) is defined as:

$$I = \frac{u'}{U} = \frac{\sqrt{\frac{1}{3}(u_x'^2 + u_y'^2 + u_z'^2)}}{\sqrt{U_x^2 + U_y^2 + U_z^2}} = \sqrt{\frac{2k}{3(U_x^2 + U_y^2 + U_z^2)}} \quad (5)$$

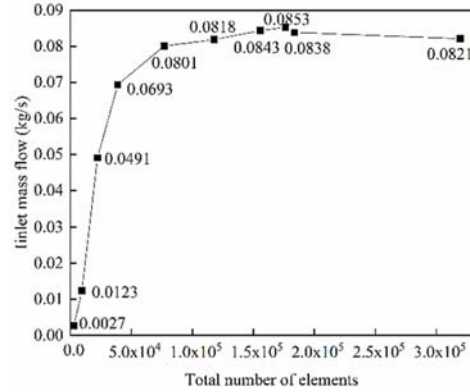


Fig. 2. Inlet mass flow with different lattice scales.

where u' is the root mean square of the turbulent velocity fluctuations; U is the mean velocity; the velocity subscripts represent the components in the X, Y and Z directions; and k is the turbulent kinetic energy.

2.4 Boundary and initial conditions

In a CFD simulation with XFlow, lattice independence verification is the first step. Under the base model of 10 mm valve lift, we selected the inlet mass flow as the judgment index to determine the appropriate lattice scale. The formula used to calculate the inlet air mass flow is shown in Eq. (6).

$$m_{inlet} = \int_{A_{inlet}} \rho V_n dA \quad (6)$$

where m_{inlet} represents inlet mass flow; A_{inlet} is inlet area; ρ is density; and V_n is the velocity normal to the inlet surfaces.

Fig. 2 shows the inlet mass flow with different lattice scales. The greater the number of elements in the initial field, the greater the consumption of computational resources. According to Fig. 2, when the number of elements exceeds 1.5×10^5 , the inlet mass flow tends to be stable. When the number of elements is 155656, the intake air flow is 0.0843 kg/s, and the minimum lattice size is 1.6 mm at this time. By the steady flow test, the average value of the inlet mass flow is 0.0837 kg/s. After comparison, the inlet mass flow of the ninth simulation is 0.0838 kg/s, and the minimum lattice size is 1.5 mm, which is closest to the test value. Therefore, the ninth simulation is taken as the optimal lattice scale. The following simulation calculations are carried out on this lattice scale.

The refinement algorithm adopts adaptive refinement. For the parts with complex structures, small sizes or of interest, different refinement regions were carried out. The refinement region indicates the border of a region with uniform resolution and the size of the cells in this region. Specific details can be found in the literature (Kui *et al.* 2019). The simulation boundary condition was the pressure boundary condition. During the test, the

flow in the intake was fully turbulent. The dimensionless flow coefficient and swirl ratio were constant. Values of the Reynolds number were greater than 60000. According to the Reynolds number similarity criterion, we obtained the relationship between the engine parameters and the minimum pressure difference of the simulated cylinder, as shown in Eq. (7):

$$\Delta p_{\min} = \left(\frac{\rho S n D^2}{60 B^2}\right)^2 \frac{1}{2\rho} \quad (7)$$

where Δp_{\min} is the minimum pressure difference; ρ is the fluid density; S is the stroke; n is the rated speed; D is the cylinder diameter; and B is the intake valve diameter.

The specific parameters of the CA4DD engine were substituted into Eq. (7) to obtain $\Delta p_{\min} = 2086$. As long as the differential pressure was greater than 2086 Pa, the test conditions were met. According to the experience of test equipment users, a differential pressure of 5000 Pa was selected. The inlet was slightly lower than atmospheric pressure and set to 99350 Pa. Therefore, the outlet differential pressure was 94350 Pa. The details of specific boundary conditions are shown in Table 4.

Table 4 Boundary conditions

Inlet	99350 Pa
Outlet	94350 Pa
Operating temperature	288.15 K
Density	1.225 kg · m ⁻³

In this test, intake-cylinder flow was approximated as turbulent flow in a pipe. The flow characteristics of each scheme were measured by the dimensionless swirl ratio and flow coefficient. These two dimensionless quantities are the ratio of vorticity and intake flow. The related physical quantities, vorticity and intake flow, were analyzed by the Buckingham theorem (García-Barrachina and Gámez 2020). The vorticity (ω) and volume flow (Q) are functions of the equivalent diameter of the model (D_e), the pressure drop (Δp), the velocity of flow (v), the flow density (ρ), the viscosity (μ), and the length (L), height (H) and the angle (θ) of the guide vane. We expressed each of these parameters with respect to the basic dimensions (MLT) and chose D_e , v and ρ as the repeating variables. Then, we constructed the dimensionless groups and wrote the final functional relationship, as shown in Eqs. (8) and (9). Since the guide vane parameters and model equivalent diameter were determined in this test, L/D_e , H/D_e and θ were constant. Equations (8) and (9) can be simplified to Eqs. (10) and (11). The swirl ratio and flow coefficient are dimensionless, and the same effects cancel. Therefore, enlarging the dimensions affects the

flow characteristics but not the results.

$$\frac{Q}{D_e^2 v} = f\left(\frac{\Delta p}{v^2 \rho}, \text{Re}, \frac{H}{D_e}, \frac{L}{D_e}, \theta\right) \quad (8)$$

$$\frac{\omega D_e}{v} = f\left(\frac{\Delta p}{v^2 \rho}, \text{Re}, \frac{H}{D_e}, \frac{L}{D_e}, \theta\right) \quad (9)$$

$$\frac{Q}{D_e^2 v} = f\left(\frac{\Delta p}{v^2 \rho}, \text{Re}\right) \quad (10)$$

$$\frac{\omega D_e}{v} = f\left(\frac{\Delta p}{v^2 \rho}, \text{Re}\right) \quad (11)$$

3. RESULTS AND DISCUSSION

3.1 Analysis of flow characteristics

In this paper, the model was simulated with different guide vane schemes and valve lifts, and the flow characteristics were analyzed. The swirl ratio and flow coefficient at 6-10 mm valve lifts were calculated. This paper used the AVL evaluation method. Two dimensionless parameters, the swirl ratio and flow coefficient, were used to characterize intake performance. The swirl ratio, which represents the ability of air to form swirls through the intake port, is defined as the ratio of swirl rotational speed (vane anemometer speed in the steady flow test) to engine simulation speed. The flow coefficient, which represents the ability of air to enter the cylinder, is defined as the ratio of the actual inlet flow through the valve seat to the theoretical inlet flow. The axial velocity of the cylinder is assumed to equal the average velocity of the piston. The swirl ratio equation can be expressed as:

$$N_s = \frac{n_D \rho V_h}{30m} \quad (12)$$

where N_s is the swirl ratio, n_D is the swirl rotational speed, V_h is the displacement, and m is the inlet mass flow.

The flow coefficient equation was expressed as:

$$C_f = \frac{Q}{i A V_0} \quad (13)$$

where Q is the volume flow, i is the number of intake valves, A is the cross-sectional area of the valve seat, and $V_0 = \sqrt{2\Delta p / \rho}$ is the theoretical intake velocity.

Table 5 shows the swirl ratio for different valve lifts and schemes. The swirl ratio increases with increasing valve lift. The guide vane improves the swirl ratio. In scheme 5 (H7.5-L50-020), the maximum average swirl ratio was 37%. Table 6 shows the flow coefficient for different valve lifts and schemes. Most of the guide vane schemes slightly reduce the flow coefficient, and the average reduction is within 5%. The guide vane has little

effect on the flow coefficient and can substantially improve the swirl ratio. Because of the trade-off relationship between the swirl ratio and the flow coefficient, the guide vane can improve the flow characteristics of the diesel engine.

Table 5 Swirl ratios for different schemes and valve lifts

Scheme	6 mm	8 mm	10 mm	Average increase, %
0	0.533	0.599	0.658	—
1	0.604	0.762	0.765	18.917
2	0.646	0.568	0.702	7.528
3	0.629	0.600	0.669	6.613
4	0.702	0.690	0.721	18.817
5	0.725	0.835	0.892	37.043
6	0.673	0.692	0.961	29.308
7	0.520	0.693	0.795	11.382
8	0.682	0.733	0.809	24.378
9	0.612	0.701	0.705	13.027

Table 6 Flow coefficients for different schemes and valve lifts

Scheme	6 mm	8 mm	10 mm	Average increase, %
0	0.462	0.549	0.574	—
1	0.459	0.546	0.585	0.172
2	0.423	0.530	0.561	-4.729
3	0.438	0.550	0.546	-3.351
4	0.447	0.531	0.548	-3.670
5	0.452	0.547	0.568	-1.249
6	0.462	0.543	0.587	0.410
7	0.443	0.532	0.566	-2.885
8	0.445	0.524	0.578	-2.521
9	0.448	0.539	0.550	-3.075

Taking the swirl ratio as the test index, the following content provides a detailed analysis of the steady flow state under the maximum valve lift for different schemes. The range of vane parameters was optimized. This paper investigated the relationship between the swirl ratio and the height, length and angle of guide vanes; this was a complex multidimensional problem. For the purpose of studying this problem simply and intuitively, this paper implemented dimensionality reduction based on feature combination. This paper defined the ratio of length to height as the aspect ratio. The data in high-dimensional space was mapped to low-dimensional space. This used fewer data dimensions and retains more characteristics of the original data points. A feature space with fewer dimensions and more independence among the dimensions was constructed. The aspect ratio of guide vane was x_1 .

The angle of guide vane was x_2 . The swirl ratio was the test index y . Table 4 shows the test results for the base model (scheme 0) and uniform design schemes.

Figure 3 shows a contour map based on Table 7. Because the various parameters of the guide vane interfered with each other, the best effect was produced only when the parameters were effectively matched. As shown in Fig. 3., the high swirl ratio was concentrated in the lower left region. A red rectangle marks the location where the swirl ratio is concentrated. The parameters in this region are better than in other areas of the map. The corresponding aspect ratio of the guide vane is in the 3.5-6.9 range, and the guide vane angle is in the 12.2°~20.2° range. When the aspect ratio and angle of the guide vane are within the above ranges, the vane can produce a better swirl effect. According to Fig. 3, the vane parameters of schemes 5, 6 and 7 are in the ranges of parameters that produce better results, which indicates that they can produce a good swirl effect.

Table 7 Results for different schemes

Scheme	Aspect ratio x_1	Angle, ° x_2	Swirl ratio y
0	0.000	0.000	0.658
1	40.000	36.000	0.765
2	15.000	32.000	0.702
3	6.667	28.000	0.669
4	10.833	24.000	0.721
5	6.667	20.000	0.892
6	3.889	16.000	0.961
7	6.667	12.000	0.795
8	4.583	8.000	0.809
9	2.963	4.000	0.705

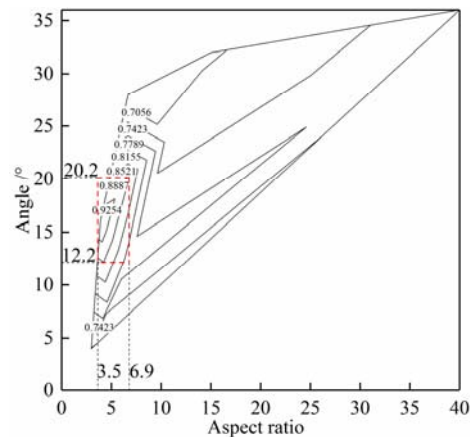


Fig. 3. Contour map of the swirl ratio.

3.2 Experimental validations

The simulation results show that scheme 5 (H7.5-L50-020) has a better effect than the other schemes on swirl. Subsequently, a steady flow test verified the simulation results. A vane anemometer and the constant pressure difference method were used to measure and calculate the flow characteristics of the intake port under fixed valve lift. The AVL evaluation method, which emphasizes the influence of the intake process on the swirl ratio and flow



Fig. 4. Steady flow test bench.

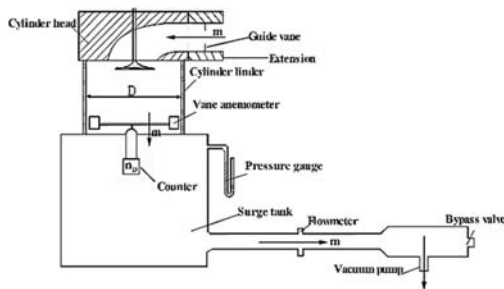


Fig. 5. Schematic of the steady-flow test bench.

coefficient, was adopted for evaluation. The steady flow test bench is shown in Fig. 4. The base model of the intake port was established according to the actual shape and printed in 3D. The schematic of the steady flow test is shown in Fig. 5. The guide vane of scheme 5 (H7.5-L50-020) was fabricated according to Table 1 and installed on the front of the helical intake port. The guide vane angle was adjusted by rotating the bolts connecting the vane. This paper used the experimental results to verify the simulation results.

Steady flow tests were conducted on schemes 0 and 5 to measure the flow coefficient and swirl ratio at 6, 8, and 10 mm valve lifts. To verify the simulation, the simulated and experimental flow characteristics were compared for high valve lifts. Fig. 6 compares the simulated and experimental swirl ratios of scheme 0 and scheme 5 at different valve lifts. There was good consistency between the simulated and experimental swirl ratios at high valve lifts, and the swirl ratio increased with increasing valve lift. The simulated swirl ratio was slightly larger than the experimental swirl ratio. The main reason is that there is no vane anemometer in the simulation, and the resistance is relatively low. Both simulated and experimental results showed that the swirl ratio of the guide vane model was greater than that of the base model. Fig. 7 compares the simulated and experimental flow coefficients of scheme 0 and scheme 5 at different valve lifts. The guide vane had little effect on the flow coefficient. The simulated and experimental flow coefficients were in good agreement. The flow coefficient increased with increasing valve lift. Compared with the base model,

the flow coefficient of the guide vane model was slightly lower, but the change was not obvious. This shows that the guide vane had a slight negative effect on the flow coefficient.

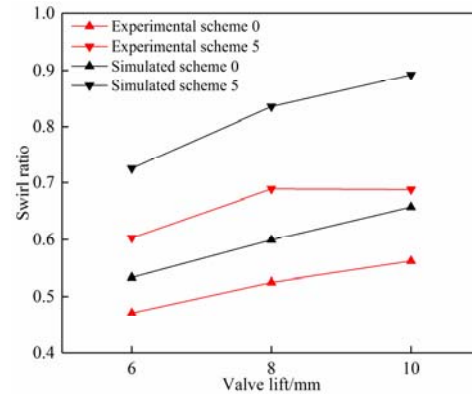


Fig. 6. Comparison of the simulated and experimental swirl ratios.

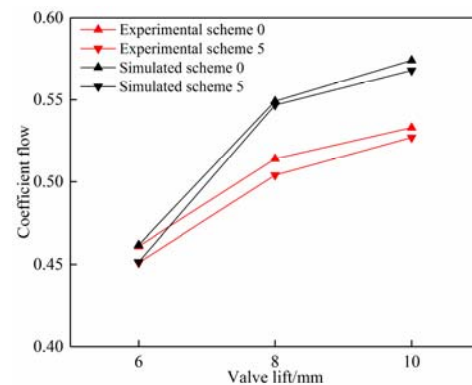


Fig. 7. Comparison of the simulated and experimental coefficient flows.

Figures 6 and 7 show that the simulated and experimental results are consistent. On the whole, the simulated results are slightly larger than the experimental results. The main reason for the slight inconsistency of the flow coefficient was the presence of the vane anemometer in the experiment. The vane anemometer consumed a certain amount of energy and produced a certain resistance, which resulted in a slight decrease in the inlet flow. The simulation was performed in the ideal fluid state and was not affected by objective conditions. In addition, the swirl in the cylinder was assumed to be a rigid body swirl. For the simulated swirl ratio, the rotational angular velocity of the rigid body was calculated by the vorticity and measured by the rotation of the vane anemometer in the test. There was a certain deviation between the simulated and experimental values. It is well known that there is a trade-off between the flow coefficient and the swirl ratio. However, the guide vane had a small effect on the flow coefficient and considerably increased the swirl ratio, which indicated that the guide vane

improved the flow characteristics of the dual-intake diesel engine.

4. FLOW FIELD ANALYSIS

XFLOW was used to simulate the intake fluid flow. The fundamental principle is to numerically solve the differential equations that control the fluid flow. The discrete distribution of the flow field in the continuous area is obtained to approximately simulate the fluid flow. Through visual postprocessing, complicated numerical solution results can be intuitively shown. The distributions of vorticity, velocity and turbulence intensity in the cylinder were analyzed at the maximum valve lift. To fully understand the flow field distribution in the cylinder, four sections were selected for each model: A-A, B-B, C-C and D-D. The position of each section is described in detail in Table 8 and shown in Fig. 8.

Table 8 Sectional position

section	Position
section A-A	1.75 times cylinder diameter
section B-B	1 mm from valve bottom
section C-C	In the middle of the intersection
section D-D	Plane of the double-valve axis

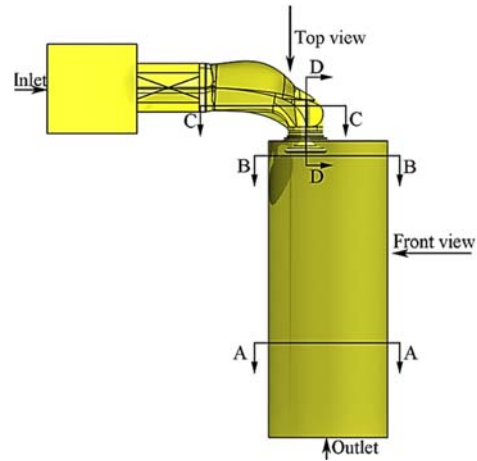


Fig. 8. Sectional position of the guide vane model.

4.1 Fluid flow in the cylinder

To clearly visualize the fluid flow in the cylinder, the simulation data were imported into EnSight. Fig. 9. shows the air streamlines for different designs in the cylinder from the front view. The positions of massless particles in the vector field are connected to construct the streamlines. In steady flow, the streamlines coincide with the traces. The density of the streamlines reflect the velocity magnitude. The

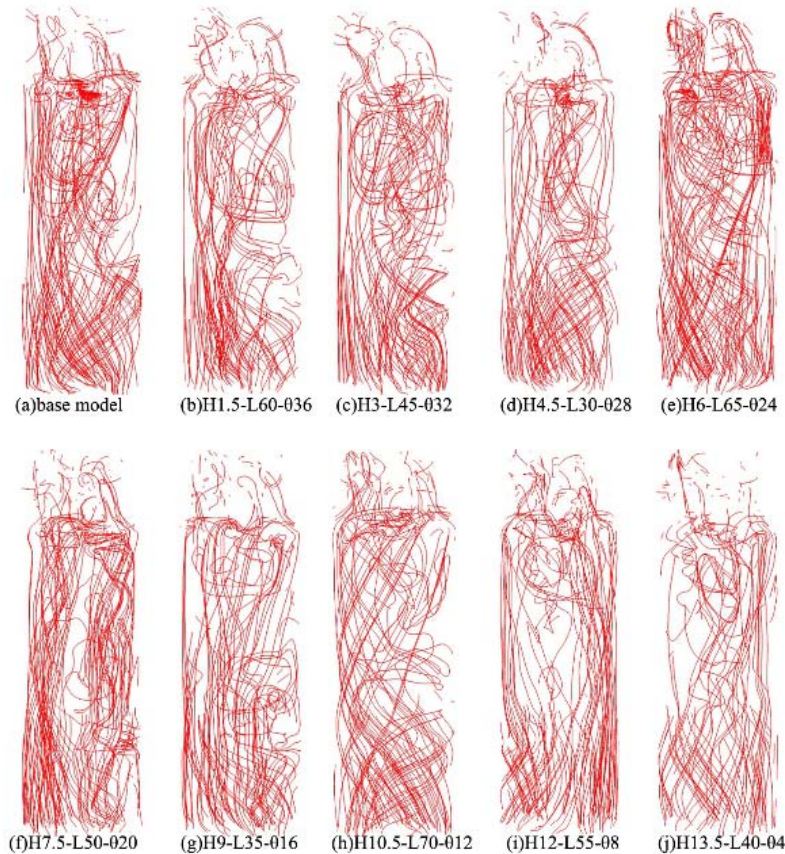


Fig. 9. Fluid flow in the cylinder for different guide vane designs.

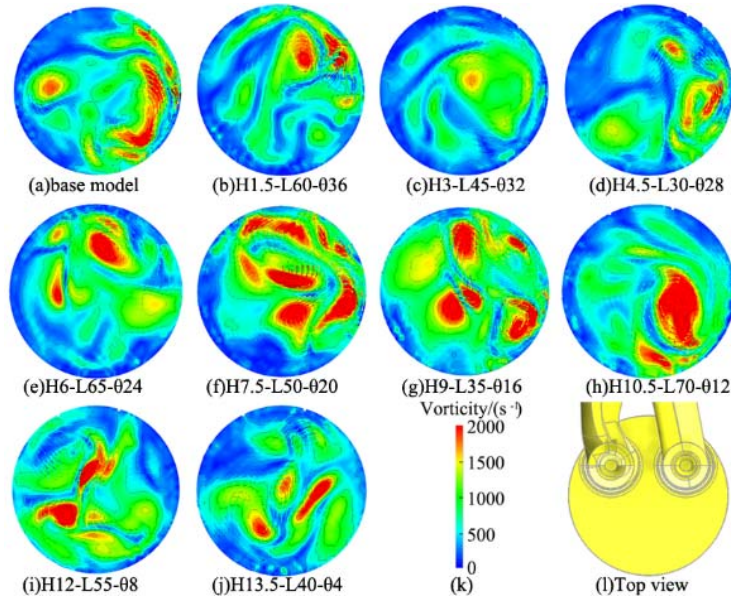


Fig. 10. Vorticity distributions for different schemes at section A-A.

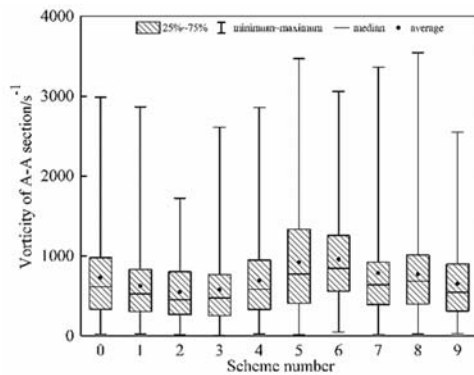


Fig. 11. Vorticity statistics for different schemes in section A-A.

spatial motion curves of the particles indicate their change in direction. Figure 9 shows that the swirl motion of the model with guide vanes is more obvious than that of the base model. The streamline density of schemes (c), (e) and (f) is obviously higher, which confirms the high velocity. Fig. 9 shows that the distribution of the streamlines in the cylinder with various guide vanes differ, i.e., different guide vanes have different impacts on the flow in the cylinder. There are small vortices in the streamlines of the base model. In the guide vane models, relatively large vortices are generated in the cylinder. The positions of the vortices are different in the various schemes. A vortex is conducive to oil-gas mixing and improves combustion efficiency.

4.2 Distribution of vorticity in the cylinder

In the steady flow test, the vane anemometer was installed at a distance of 1.75 times the diameter from the cylinder top. The swirl ratio was calculated by measuring the speed of the vane anemometer. Therefore, the vorticity of the A-A section was selected for analysis. Swirl is a structural form of the

vorticity field. The intake swirl can exist during the entire intake process, even in the process of compression and expansion (Song *et al.* 2015). Its sharp rotational motion can be used for well-organized air movement in cylinders, which can improve the rates of mixing and combustion as well as the combustion quality. Fig. 10 shows the vorticity distributions of various schemes at section A-A, where (a)-(j) correspond to the vorticity distribution of schemes 0-9, (k) is the color scale, and (l) is the view position when the vorticity field is selected. The flow field is colored according to the magnitude of the field in the cutting plane. The vorticity vectors are visualized on the section, which are represented by the density and length of the arrows. The isocontours are shown on the section. As shown in Fig. 10, scheme 5 (H7.5-L50-020) obviously has more areas with greater vorticity compared with the basic model. Scheme 7 (H10.5-L70-012) has a distinct area of high vorticity. The vorticity distributions of the other schemes differ considerably from that of the base model, which indicates that the guide vanes greatly influenced the flow field distributions. Fig. 11 is a boxplot of the vorticity for each scheme. The minima are similar. Compared with the base model, the average and maximum vorticities of schemes 5-8 increase, while those of other schemes undergo relatively small changes. Scheme 6 (H9-L35-016) has the largest average vorticity and relatively concentrated data, but the upper limit of the vorticity is limited. Scheme 5 (H7.5-L50-020) has the second highest average, and the data fluctuate in a larger range.

4.3 Distribution of velocity in the cylinder

Section B-B was used to evaluate the velocity distribution at a distance of 1 mm from the bottom of the valve. Fig. 12 shows the velocity distribution for different schemes in section B-B. The arrangement of Fig. 12 is similar to that of Fig. 10.

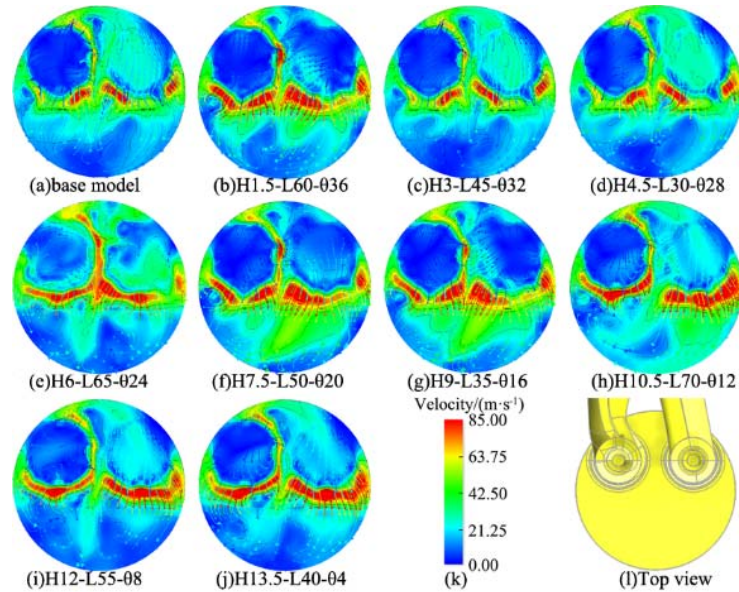


Fig. 12. Velocity distributions for different schemes in section B-B.

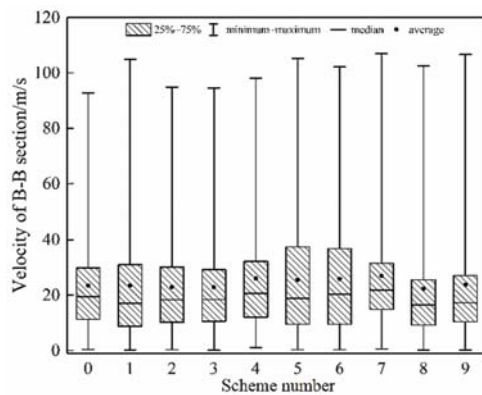


Fig. 13. Velocity statistics for different schemes in section B-B.

Compared with the base model, the guide vane model forms a high-speed area around the intake valve, especially the spiral intake valve. The valve head hinders the collection of high-speed fluid. On the vertical plane between the two intake valves, the flow field distribution is mostly symmetrical. Fig. 13. is a boxplot of the velocity statistic for different schemes in section B-B. Compared with the base model, the averages of schemes 4-7 are much higher. Scheme 7 (H10.5-L70-012) has the largest average. The growth rate is 14.6%, and the data are relatively concentrated with little fluctuation. The growth rate of scheme 4 (H6-L65-024) is followed by scheme 7. The averages of the other schemes show relatively small changes. The maximum of each scheme is higher relative to that of the base model, and the growth rate ranges from 2.1 to 15.4%. The statistical values of different schemes are similar. Most guide vane models increased the velocity in this region.

4.4 Distribution of velocity in the intake port

Section C-C was used to evaluate the velocity distribution in the middle position where the intake port intersects with the valve stem. Fig. 14. shows the velocity distribution for different schemes at section B-B. The arrangement of Fig. 14 is similar to the Fig. 10. When the shape of the helical intake port changes, the velocity increases. In the flow direction, the shape of the intake port suddenly narrows, and the flow direction changes to increase the velocity, which is consistent with the Bernoulli law. Compared with the base model, the high-speed areas of scheme 1 (H1.5-L60-036), scheme 5 (H7.5-L50-020) and scheme 6 (H9-L35-016) are significantly increased at the helical intake. In other schemes, the high-speed area of the helical intake is slightly reduced. Due to the mutual interference of the airflow, the flow field distribution of the tangential intake port also changes. The helical intake port makes the airflow spiral motion, so the low-speed area is concentrated on the side of the valve stem. The tangential intake port does not produce a spiral effect, and the low-speed area is concentrated in front of the valve stem. These two areas are where the airflow meets after bypassing the valve stem. For the helical intake port, the farther back of the low-speed area, the better the spiral effect. Fig. 15. is the boxplot of the velocity statistics for different schemes at the C-C section.

4.5 Distributions of valve flow fields

The D-D section was the plane where the axes of the two intake valves were located, and it was cut to a distance of 10 mm from the bottom of the intake valve. Fig. 16. shows the velocity distribution for different schemes at section D-D. The arrangement

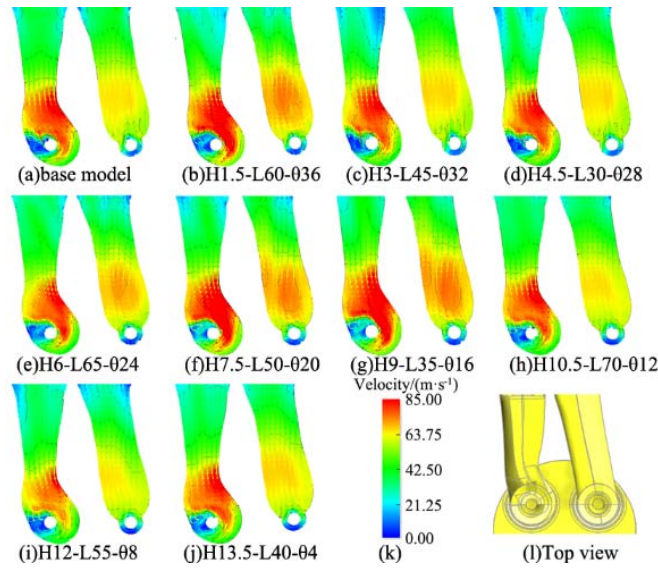


Fig. 14. Velocity distributions for different schemes at the C-C section.

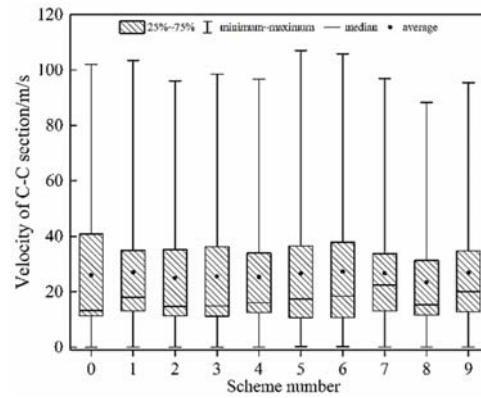


Fig. 15. Velocity statistics for different schemes in section C-C.

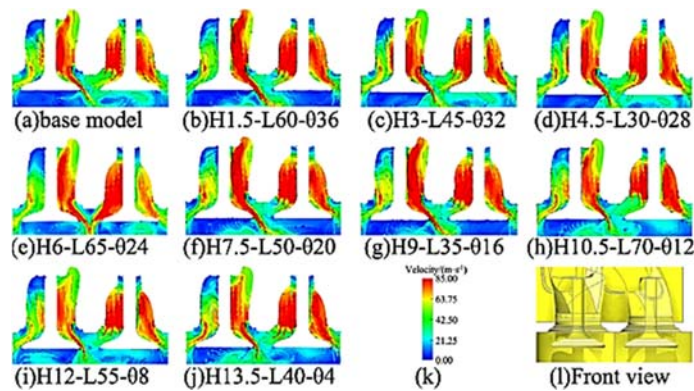


Fig. 16. Velocity distributions for different schemes in section D-D.

of Fig. 16 is similar to the Fig. 10. In the helical intake port, the velocity on the left side of the valvestem is relatively low, which is the same as that in Fig. 16. The main reason is that the airflows joined after bypassing the valve stem and flowed in

opposite directions. Therefore, the energy partially canceled, and the dominant fluid movement was observed. Because of the spiral effect of the helical intake port, the flow direction of the intake air changed, and the fluid flowed into the cylinder at a

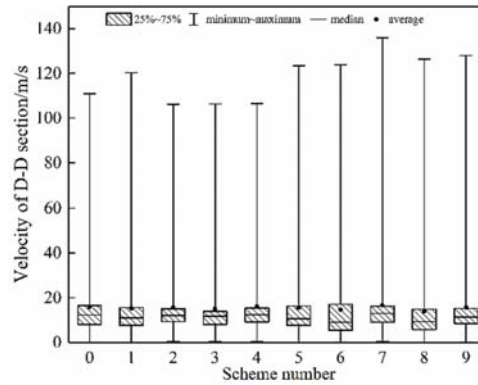


Fig. 17. Velocity statistics for different schemes in section D-D.

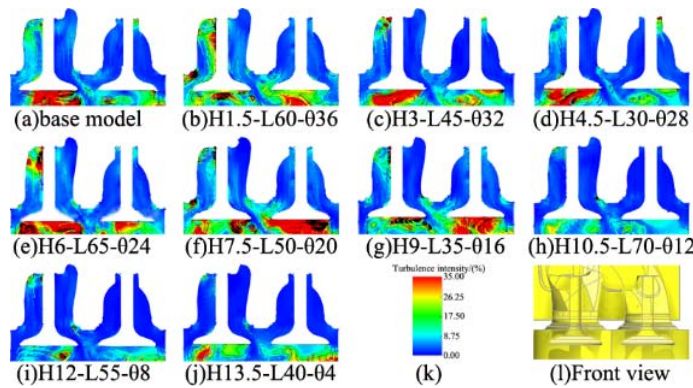


Fig. 18. Turbulence intensity distributions for different schemes in section D-D.

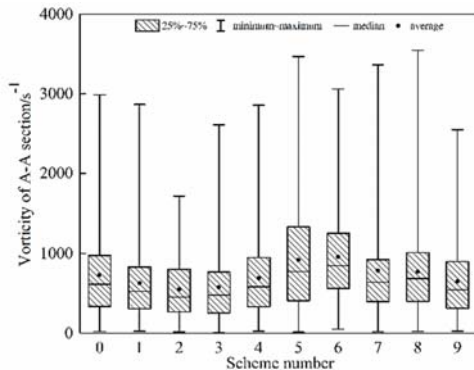


Fig. 19. Turbulence intensity statistics for different schemes in section D-D.

certain velocity. The conical jet violently impacted the cylinder wall. Consequently, the jets that located on the right side of the helical intake and the left side of the tangential intake interfered and merged in the middle to form a high-speed area. Compared with the base model, the guide vane model influenced the flow direction. Fig. 17. is the boxplot of the velocity statistic for different schemes in section D-D. Fig. 17. shows that the data statistics in this area slightly

differed and fluctuated. The average is greatly affected by bigger values. Scheme 1 (H1.5-L60-036), scheme 5 (H7.5-L50-020) and scheme 6 (H9-L35-016) have an obvious high-speed jet area increase on the right of the helical intake port. On the left side of the tangential intake port, the high-speed area of scheme 4 (H6-L65-024) increases significantly. High speed can increase the air-fuel mixing rate and the combustion efficiency.

The turbulence intensity is defined as the ratio of the root mean square of the turbulence velocity fluctuations to the mean velocity. The turbulence intensity is one of the important properties that supply jets (Cao *et al.* 2013). Fig. 18. shows the turbulence intensity distribution for different schemes at section D-D. The arrangement of Fig. 18 is similar to the Fig. 10. The turbulence intensity on the left side of the helical intake port is relatively high. In the cylinder, the turbulence intensity is high and very uneven. There are great changes among different schemes, especially at the interference of helical and tangential airflow. The turbulence intensity under the intake valve fluctuates greatly. In schemes 3-6, the turbulence intensity concentration areas increase substantially compared with the base model. Figure 19. is the boxplot of the turbulence intensity statistic for different schemes in section D-

D. Figure 19. shows that all data of each scheme are distributed symmetrically. The data distribution is uniform and concentrated. In scheme 2 (H3-L45-032), scheme 3 (H4.5-L30-028) and Scheme 7 (H10.5-L70-012), the turbulence intensity is slightly reduced compared with the base model. The turbulence intensity of other schemes is obviously increased. Scheme 5 (H7.5-L50-020) has the maximum average value with a growth rate of 49.1%.

5. CONCLUSION

- (1) Guide vane models with different parameters were established to simulate the effects of guide vanes on the dual-intake port diesel engine flow characteristics at high valve lifts. This study provides a theoretical basis for improving diesel engine efficiency and energy savings.
- (2) The optimal range of vane parameters under the maximum valve lift was determined by parameter dimension reduction. When the vane aspect ratio was 3.5-6.9 and the vane angle was 12.2°-20.2°, the effect of the swirl ratio was the best.
- (3) The flow field distribution of all schemes was analyzed at the maximum valve lift. Most of the guide vane models improved the flow field distribution. Scheme 5 (H7.5-L50-020) had the best comprehensive effect on the flow field distribution.
- (4) The simulation results were verified by a steady flow test. The simulated and experimental results displayed good consistency. Compared with the base model, the maximum average increase in the swirl ratio was 37%, and the flow coefficient fluctuated within 5%. Both the swirl ratio and flow coefficient increased with increasing valve lift.

REFERENCES

- Bari, S. and I. Saad (2014). Effect of guide vane height on the performance and emissions of a compression ignition (CI) engine run with biodiesel through simulation and experiment. *Applied Energy* 136, 431-444.
- Bari, S. and I. Saad (2015a). Optimization of vane numbers through simulation and experiment, and investigation of the effect on the performance and emissions of a CI (compression ignition) engine run with biodiesel. *Energy* 79(C), 248-263.
- Bari, S. and I. Saad (2015b). Performance and emissions of a compression ignition (CI) engine run with biodiesel using guide vanes at varied vane angles. *Fuel* 143, 217-228.
- Bari, S. and I. Saad (2016). Simulation and Experimental Investigation of Guide Vane Length to Improve the Performance of a Diesel Engine Run with Biodiesel. *Journal of Engineering for Gas Turbines and Power* 138(11).
- Bayramoglu, K., S. Yilmaz and K. D. Kaya (2019). Numerical investigation of valve lifts effects on performance and emissions in diesel engine. *International Journal of Global Warming* 18(3-4), 287-303.
- Cao, G., C. Kandzia, D. Müller, J. Heikkinen, R. Kosonen and M. Ruponen (2013). Experimental study of the effect of turbulence intensities on the maximum velocity decay of an attached plane jet. *Energy and Buildings* 65, 127-136.
- Evans, B., M. Hanna, M. Dawson and M. Mesiti (2019). High order parallelisation of an unstructured grid, discontinuous-Galerkin finite element solver for the Boltzmann-BGK equation. *International Journal of Computational Fluid Dynamics* 33(8), 343-351.
- Fang, K. T., M. Q. Liu, H. Qin and Y. D. Zhou (2018). Construction of Uniform Designs—Algorithmic Optimization Methods. *In Theory and Application of Uniform Experimental Designs* (pp. 155-182)
- Gao, Y., Y. Yu, L. Yang, S. Qin and G. Hou (2021). Development of a coupled simplified lattice Boltzmann method for thermal flows. *Computers & Fluids*.
- García-Barrachina, L. and A. J. Gámez (2020). Dimensional Analysis of Superplastic Processes with the Buckingham Π Theorem. *Metals* 10(12).
- Han, M., R. Ooka and H. Kikumoto (2019). Lattice Boltzmann method-based large-eddy simulation of indoor isothermal airflow. *International Journal of Heat and Mass Transfer* 130, 700-709.
- Hausmann M., F. Ries, J. B. Jeppener-Haltenhoff, Y. Li, M. Schmidt, C. Welch, L. Illmann, B. Bohm, H. Nirschl, M. Krause, A. Sadiki. (2020). Evaluation of a Near-Wall-Modeled Large Eddy Lattice Boltzmann Method for the Analysis of Complex Flows Relevant to IC Engines. *Computation* 8(2):43.
- Jia, D. W., X. W. Deng and J. L. Lei (2018). Steady-State Experiment and Simulation of Intake Ports in a Four-Valve Direct Injection Diesel Engine. *Journal of Applied Fluid Mechanics* 11(1), 217-224.
- Jia, D. W., X. W. Deng and J. L. Lei (2019). Intake Flow Interference Analysis of Combination Intake Port in Diesel Engine. *Journal of Applied Fluid Mechanics* 12(1), 61-67.
- Jonnalagadda A., A. Sharma and A. Agrawal. (2021). Single relaxation time entropic lattice Boltzmann methods: A developer's perspective for stable and accurate simulations. *Computers & Fluids* 215.
- Kui, H., Y. Guo, P. Cheng, C. Fu, X. Liu and G. Li (2019). Research on the flow characteristics of diesel engine with helical intake port based on

- XFLOW. 19th COTA *International Conference of Transportation Professionals: Transportation in China - Connecting the World*, CICTP 2019, July 6, 2019 - July 8, 2019 (pp. 4097-4106). Nanjing, China: American Society of Civil Engineers (ASCE).
- Kui, H., H. Wang, W. Ni, Y. Chen and J. Li (2014). Flow characteristics in diesel helical intake port bionic with non-smooth surface. *Jilin Daxue Xuebao (Gongxueban)/Journal of Jilin University (Engineering and Technology Edition)* 44(3), 668-674.
- Kumar, C. S., S. Mohankumar, M. Geier and A. Pattamatta (2017). Numerical investigations on convective heat transfer enhancement in jet impingement due to the presence of porous media using Cascaded Lattice Boltzmann method. *International Journal of Thermal Sciences* 122, 201-217.
- Leung, Y. W. and Y. P. Wang (2000). Multiobjective programming using uniform design and genetic algorithm. *Ieee Transactions on Systems Man and Cybernetics Part C-Applications and Reviews* 30(3), 293-304.
- Li, H., G. Li, Y. Yu, R. Gao, P. Zhao and Y. Yuan (2012). Effects of intake pressure difference on the flow near valve seat in diesel engine using three dimensional computation (Inner Mongolia U., Trans.). 1st *International Conference on Energy and Environmental Protection (ICEEP 2012)* (Vol. 516-517, pp. 598-601). Hohhot, PEOPLES R CHINA.
- Liu, J. and Y. Li (2012). An improved adaptive response surface method for structural reliability analysis. *Journal of Central South University of Technology* 19(4), 1148-1154.
- Liu, J., Y. Yu, C. Zhu and Y. Zhang (2021). Comparison of LBM and FVM in the estimation of LAD stenosis. *Proc Inst Mech Eng H*. 9544119211016912.
- Long, Y., X. Long, B. Ji and T. Xing (2019). Verification and validation of Large Eddy Simulation of attached cavitating flow around a Clark-Y hydrofoil. *International Journal of Multiphase Flow* 115, 93-107.
- Sharma, K. V., R. Straka and F. W. Tavares (2020). Current status of Lattice Boltzmann Methods applied to aerodynamic, aeroacoustic, and thermal flows. *Progress in Aerospace Sciences* 115.
- Song, J., G. Lv, C. Song and T. Wang (2015). Fluid flow in internal combustion engines. Tianjin: Tianjin university press, Tianjin, China.
- Szpica, D. (2020). Determination of Low Pressure Gas Injector Valve Flow Factor. *Journal of Engineering for Rural Development - International Scientific Conference*. 721-729.
- Tiwari, P., Z. Xia and X. Han (2020). Comparison of VLES and LES Turbulence Modeling for Swirling Turbulent Flow. *Journal of Applied Fluid Mechanics* 13(4), 1107-1116.
- Wang, G., W. Yu, X. Li and R. Yang (2020). Influence of fuel injection and intake port on combustion characteristics of controllable intake swirl diesel engine. *Fuel* 262.
- Wang, T., D. Liu, G. Wang, B. Tan and Z. Peng (2015). Effects of Variable Valve Lift on In-Cylinder Air Motion. *Energies* 8(12), 13778-13795.
- Xiao, T. and M. Frank (2021). A stochastic kinetic scheme for multi-scale flow transport with uncertainty quantification. *Journal of Computational Physics* 437.
- Xin, X., D. Liu, L. Wang and L. Wang (2012). Influence of variable swirl intake manifolds for di diesel engine on in-cylinder air motion. 2011 3rd International Conference on Mechanical and Electronics Engineering, ICMEE 2011, September 23, 2011 - September 25, 2011 (Vol. 130-134, pp. 95-98). Hefei, China: Trans Tech Publications.
- Zhang, J., X. Zhu, J. Feng and Y. Yang (2019). Finding community of brain networks based on artificial bee colony with uniform design. %J *Multimedia Tools & Applications*. Vol.78 (No.23), 33297-33317.